JOURNAL OF APPLIED ELECTROCHEMISTRY 24 (1994) 658–665

Local enhancement of liquid-to-wall mass transfer by a single gas bubble

A. BEN YOUSSEF, U. HAEBEL, PH. JAVET

Institute of Chemical Engineering, Swiss Federal Institute of Technology, CH-1015 Lausanne, Switzerland

Received 10 May 1993; revised 15 February 1994

Local liquid-to-wall mass transfer enhancement by a single bubble was studied. Both photographic and local current measurements were taken. The effects of the bubble form, wake and trajectory were analysed for vertical and down-facing inclined electrodes. For angles lower than 40°, bubbles rise over the surface with small hops of regular amplitude. High current increases were observed where the bubble hits the electrode. For higher angles, the bubble glides, producing high constant currents.

List of symbols

A	electrode surface area (cm^2)
c_b	concentration in bulk ($mol\,cm^{-3}$)
D	diffusivity ($cm^2\,s^{-1}$)
D_{eq}	bubble equivalent diameter (cm)
D_{tr}	bubble transverse diameter (cm)
F	Faraday's constant ($A\,s\,mol^{-1}$)
i	current density ($A\,cm^{-2}$)
I_{nc}	natural convection limiting current (A)
$\bar{I}_{max}$	current peaks averaged on the nine MEs (A)
k	mass transfer coefficient ($cm\,s^{-1}$)
M	Morton number, $g\nu^4\rho^{-1}\sigma^{-3}$
n	valence change in electrochemical reaction
Re	Reynolds number, $\rho V D_{eq}\mu^{-1}$
t	time (s)
V	bubble velocity ($cm\,s^{-1}$)

Greek symbols

α	inclination angle (degree)
ρ	liquid density ($g\,cm^{-3}$)
μ	dynamic viscosity ($g\,cm^{-1}\,s$)
ν	kinematic viscosity ($cm^2\,s^{-1}$)
σ	surface tension ($g\,s^{-2}$)

1. Introduction

Gas bubble stirring is an attractive technique in electrochemical cells where mass transfer limits the reaction rate. Several forms of agitation, such as directed convection, moving electrodes and ultrasonic agitation, have been studied by investigators in laboratory-scale cells [1, 2]. However, the use of the buoyancy force to promote mixing and reduce the diffusion layer thickness is preferred in industrial electrochemical processes because of the advantages of cheap agitation costs, simple construction and high mass transfer coefficients. The enhancement of average rates of mass transfer by gas sparging has been extensively studied [3–5]. Nevertheless, because of the global approaches generally followed, most investigators have presented their results as dimensionless correlations showing the dependence of average mass transfer rates on gas void fraction in cells with relatively large active surfaces [6–13]. These correlations are useful for estimating the mass transfer coefficient in gas sparging systems, but they do not provide insight into the mechanisms of mass transfer enhancement or a measurement of the effects on current densities of bubble distribution, trajectory and wake.

This paper was presented at the International Workshop on Electrodiffusion Diagnostics of Flows held in Dourdan, France, May 1993.

The use of global methods in dealing with bubble-driven fluid flows in electrochemical cells leads to the emergence of two groups of mathematical models. The first group assumes that the enhanced effect produced by gas bubbles is related to the removal of a surface film from the transfer surface by eddies caused by bubbles moving near the wall. For this case, treatments have been developed in the context of surface renewal theory [14–16]. The Cottrell equation in a stagnant medium was used as the basic equation:

$$i(t) = nFc_b\sqrt{\left(\frac{D}{\pi t}\right)} \quad (1)$$

The second group assumes that the mass transfer enhancement results from an increase in the velocity gradient within the vicinity of the electrode, owing to the downstream liquid flow originated by the discontinuous phase which is more concentrated in the centre of the column [11, 16].

By focusing on the behaviour of a single bubble and using small active surfaces to measure local current densities, it is possible to identify the key factors in reactant replenishment near the electrode surface and to quantify the bubble trajectory and wake effect.

Previously, in this laboratory, Larpin studied the induced enhancement of a single bubble through the motion of rigid spheres (steel balls) rolling in a controlled manner in the vicinity of a flat electrode

0021-891X

in an initially motionless electrolyte. A model involving exponential decrease of turbulent perturbations both in time and distances was proposed [17].

The present work aims to resolve, spatially and temporally, the mass transfer resulting from the passage of a bubble close to a microelectrode (ME), such that the enhancement can be locally characterized. The objective is to correlate the variations of local currents with the dimensions and the distance of separation of the bubble from the ME.

Preliminary measurements with electrodes in a vertical surface have shown poor reproducibility of ME responses to the perturbations caused by the passage of the bubble. It was therefore decided to use electrodes inclined at different angles, so that the buoyancy force causes the bubble to pass close to the ME. Special attention was then given to the trajectory of the bubble near the ME in the vertical cell and to the nature of its wake, which is believed to have a direct impact on the transport phenomena.

Except for the work of Tobias and Whitney [16] on mass transfer of microbubble streams rising near vertical electrodes, no other study using such an approach has been reported.

2. Experimental details

The limiting current technique was employed. The reduction of ferricyanide ion was used and currents to the big cathode and to the MEs were monitored by a data acquisition and control system. The electrolytic solution was 0.025 M in potassium ferro and ferricyanide, and 2 M in NaOH. Mass transfer coefficients were derived from the values of the limiting current using

$$k = \frac{I_{nc}}{c_b AF} \qquad (2)$$

The electrode consisted of a 25 cm^2 nickel-plated copper square sheet with 13 insulated MEs. The diameter of the active area of each ME was 0.62 mm and the insulation was 0.12 mm thick. Figure 1 shows how the MEs were positioned in the big cathode. The distances between two MEs were 3 mm for the horizontal row and 10 mm for the vertical row, respectively. The counter electrode was a rectangular 6 cm × 15 cm nickel sheet.

A schematic diagram of the cell with electrodes in the vertical position is shown in Fig. 2. The glass tube was 80 cm high to allow the bubble to reach its critical velocity; its diameter was 8 cm. The cell had a parallelepiped form. It was made of PVC and sealed to the tube, and was designed to accommodate both a photographic system and the cathode with its MEs in a vertical position. The cathode was fixed on one side, with each of the three other sides having a window allowing lighting and positioning of a photodetector. The experiments were performed

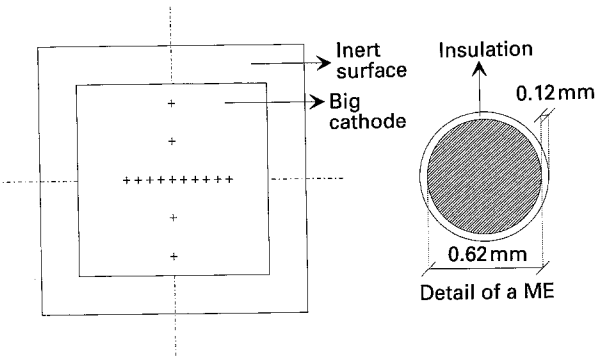

Fig. 1. Test electrode.

in darkness. A cylindrical lens placed in front of a He–Ne laser source focussed the beam into a horizontal light sheet (~ 1 mm thick) that passed through one window and lit the horizontal row of MEs. The light reflected by the gas bubble crossing this sheet was measured by a photodetector fixed in another window. The photodetector was connected to an acquisition card that triggered a flash so that when the bubble passed in front of the horizontal row of MEs, a camera positioned above the cell took a picture. This yielded the dimensions and the position of the bubble relative to the MEs with high accuracy. The same equipment was also positioned at a lower level in the tube in order to determine the velocity of the bubble in the electrolyte.

For experiments with electrodes in inclined positions, the 60 cm × 17 cm × 5 cm Plexiglas® parallelipedal cell

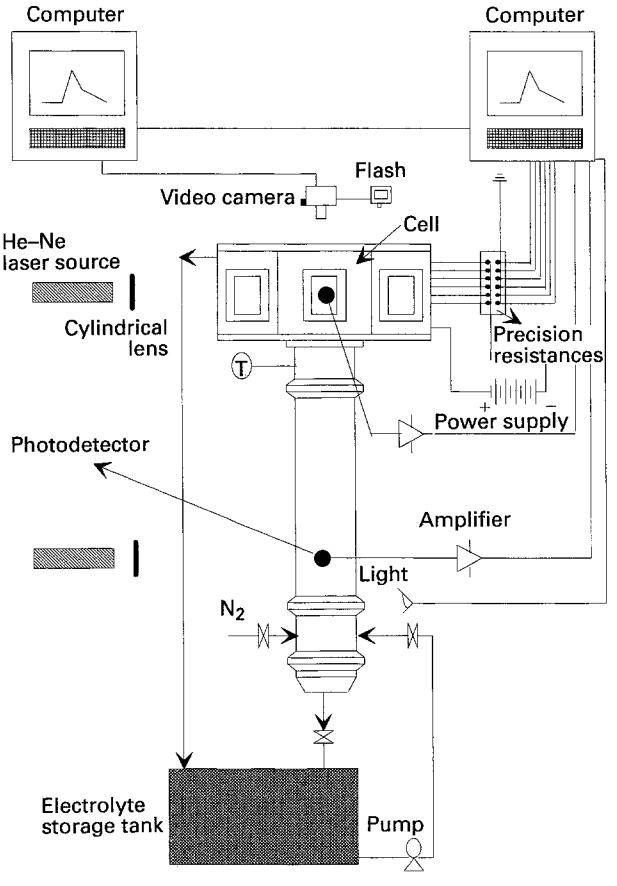

Fig. 2. Experimental setup.

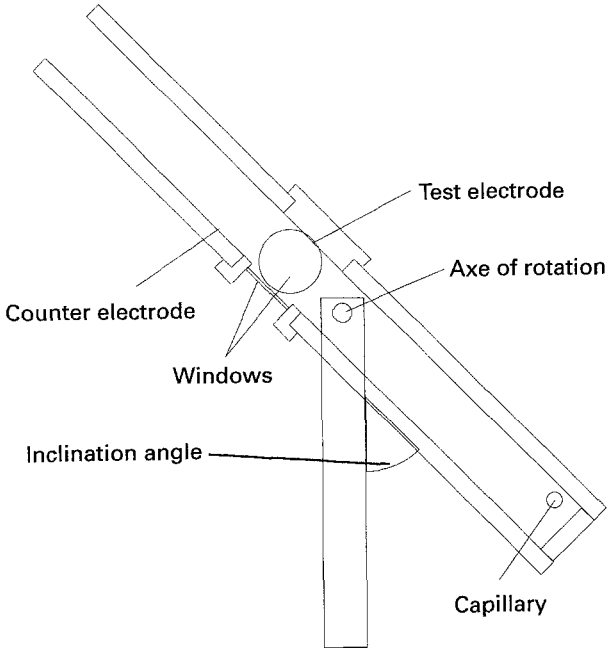

Fig. 3. Cell of variable inclination.

shown in Fig. 3 was used. The whole cell pivoted around an axis parallel to the electrodes, so that the test electrode faced down at different angles. The same measurement system used for the installation previously described was applied.

Nitrogen bubbles were formed using glass capillaries as described by Blanchard *et al.* [18].

3. Results

3.1. *Bubble behaviour*

The equivalent diameter is usually used as the characteristic length to study the evolution of a bubble in a stagnant medium. The shape is fixed by the relative intensity of the gravitational, buoyancy, and drag forces. It passes from a sphere to a spheroid which becomes flatter and flatter as its volume increases. Bubbles of larger volume have a spherical-cap form. The volumes at which these transitions happen depend on the Morton number [19–21]. This number is 1.64×10^{-10} for the electrolytic solution used.

Figure 4 shows typical examples of these three ranges; it represents the bubbles observed from the window placed in front of the cathode, and allows determination of the longitudinal and transverse dimensions. The symmetry of the bubble offers the possibility of calculating the equivalent diameter using the formulae presented in Fig. 5.

Figure 6 presents two bubbles of the third category of the same equivalent diameter taken at the same level in the column. It shows that the observed form of this type of bubble is only instantaneous and is not constant during its rise. To determine the equivalent diameter of these bubbles a certain number of them was collected in a graduated cylinder.

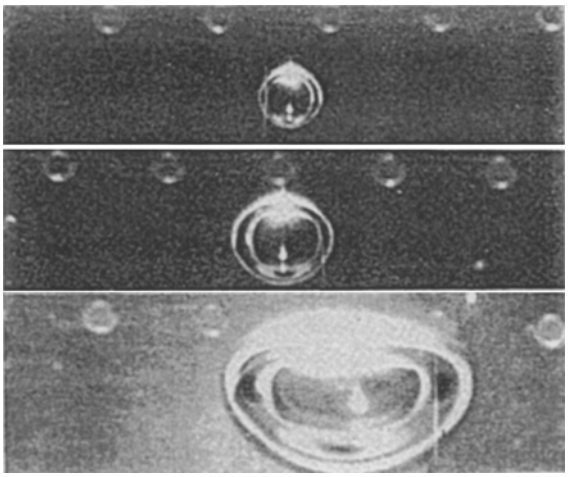

Fig. 4. Examples of typical bubble forms. (Intermicroelectrode distance visible behind the bubbles: 3 mm).

The following correlation (3) between transverse and equivalent diameters has been established for spheroidal bubbles:

$$D_{tr} = 1.19\, D_{eq}^{1.06} \qquad (3)$$

This expression was obtained from Fig. 7 and is valid for equivalent diameters between 0.8 and 4.5 mm.

Bubble velocity measurements were taken by placing a system composed of a laser He–Ne source, a cylindrical lens, a photodetector, and an amplifier at two different levels in the column. The amplified signals were transferred and stored by the acquisition chain. The first system was placed far enough from the bubble formation capillary so that bubbles were already at their critical velocities when passing through the lower light sheet. Bubble dimensions were determined from the pictures taken

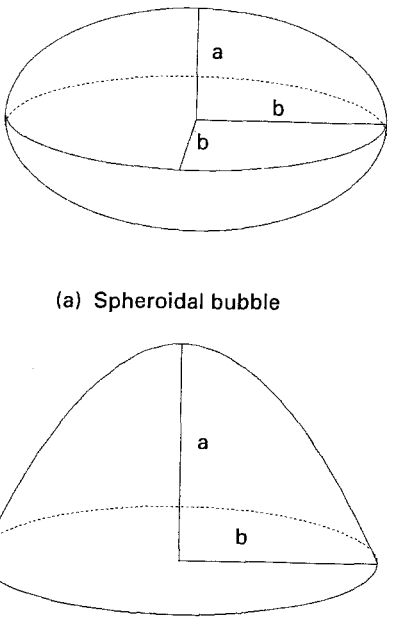

Fig. 5. Formulae used to calculate bubble volume: (a) $V = \frac{4}{3}\pi b^2 a$; (b) $V = \frac{1}{2}\pi b^2 a$.

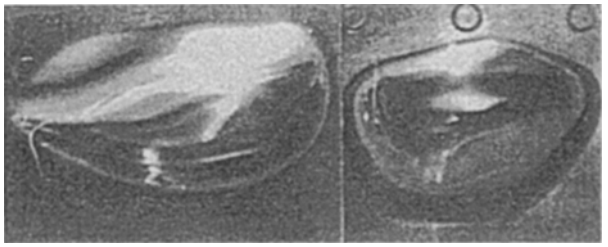

Fig. 6. Example of bubble interfacial vibration. (Intermicroelectrode distance, visible behind bubbles: 3 mm).

when they crossed the upper light sheet and from Correlation 3.

Experimental studies of measurements of bubble velocity as a function of equivalent diameter in pure liquids shows a maximum. This corresponds to the transition from a viscous flow regime to an inertial flow regime, which implies a transition of the spheroidal form to the spherical-cap form. Haberman and Morton [21] have measured bubble velocities in tap water, as well as in water containing small concentrations of surfactants. They observed that velocities of spherical bubbles and spherical-cap bubbles agree with those obtained in filtered water. This is not the case with spheroidal bubbles; the velocity curves no longer show a peak. This was explained by the accumulation of impurities or surfactant molecules on the bubble surface, that confer a higher rigidity.

The curve in Fig. 8 shows the results obtained in the present work; its strictly monotone aspect, in contrast with results for pure liquids from the literature, is justified by the phenomenon described above.

The use of a multiburst flash triggered by the acquisition and control chain allowed visualization of the trajectory of the bubble by creating a series of images on a single frame. The flash was timed to produce ten bursts at a frequency of 50 Hz, beginning when the bubble reached the vision field of the camera; the laser sheet was placed at the lower limit of this field. Figure 9 presents three examples of different trajectories observed for bubbles whose equivalent diameters were in the ranges of interest.

Change occurs from a rectilinear trajectory for bubbles of very small diameter to a helicoidal

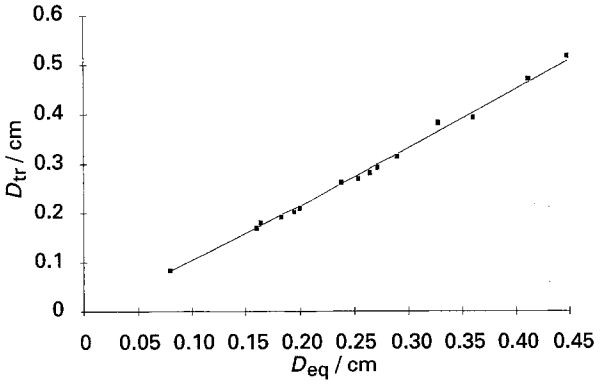

Fig. 7. Transversal against equivalent diameter.

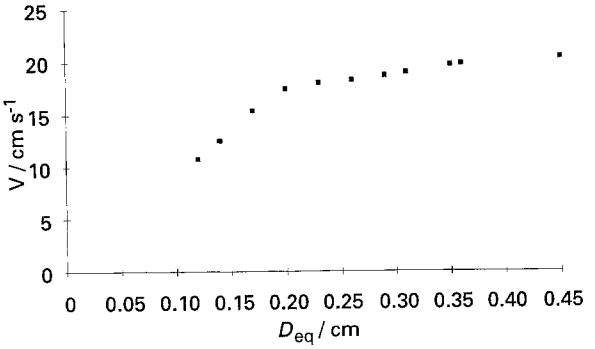

Fig. 8. Velocity against equivalent diameter.

trajectory for larger bubbles. For spheroidal bubbles, the radius of the helix made by the bubble increased with Reynolds number up to a maximum, and the transverse diameter always remained perpendicular to the direction of the movement. Large fluctuations of the liquid–gas interface appear with increasing bubble size. These are visible in Fig. 9 for the biggest bubble, which has a tendency towards break-up, and a helical thread longer than that for spheroidal bubbles.

3.2. *Perturbation on an inclined electrode*

Different trajectories were observed when bubbles rise close to an inclined electrode. (a) For small angles, up to 35°, all the bubbles rise by small hops, bouncing over the wall (Fig. 10). (b) For angles superior to 45°, they glide over the wall. (c) For intermediate angles, the irregularities of the wall make the trajectory unpredictable because the

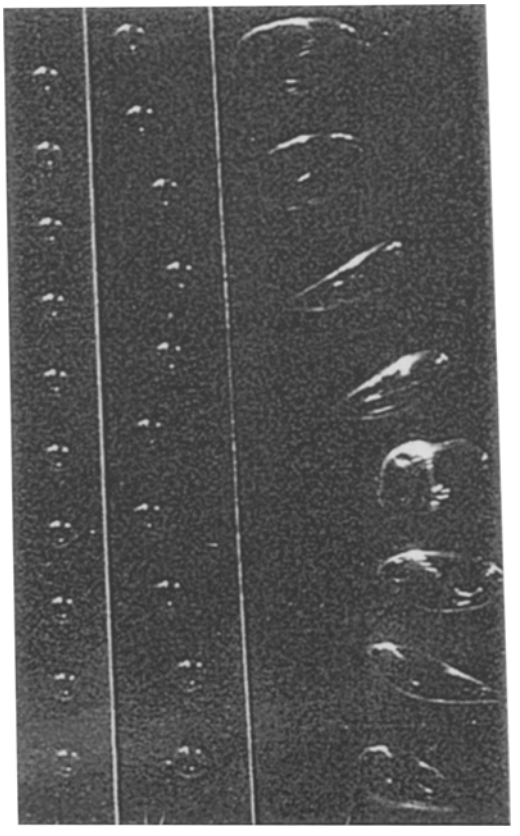

Fig. 9. Examples of typical trajectories.

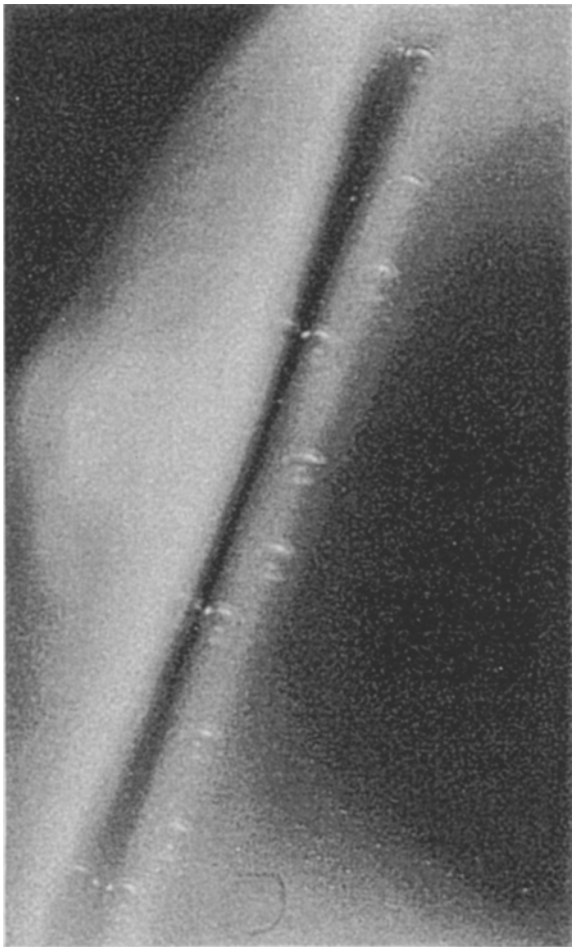

Fig. 10. Rise of a bubble close to an inclined electrode. ($D_{eq} = 1.35$ m, $\alpha = 20°$).

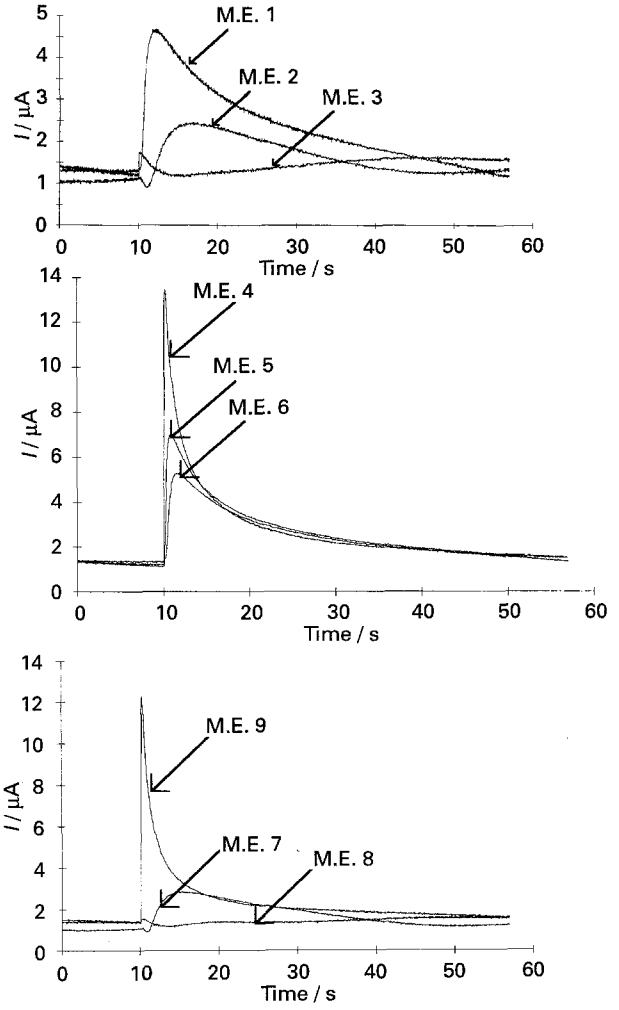

Fig. 11. Signals of the nine MEs after the rise of a bubble. ($D_{eq} = 2.2$ mm, $\alpha = 15°$).

influence of these defects was more important in this zone.

The local determination with a ME of the convection provoked by the passage of a bubble becomes more delicate when the bubble hops over the electrode. In fact, the response registered on the ME is different depending on whether the bubble bounces, or not, on the electrode. An electrode with nine MEs was installed parallel to the bubble trajectory. Figure 11 shows the responses obtained with this arrangement for the passage of a bubble ($D_{eq} = 2.2$ mm) at 15° inclination. The MEs are numbered from the bottom up. The bubble passes in front of the electrode almost 10 s after data acquisition is initiated. The bubble bounced on MEs No. 4 and 9. The perturbation generated on ME 4 decreased on MEs 5–8. On the other hand, ME 3, placed just before the point of impact of the bubble, was not perturbed.

Figure 12 shows the maximum currents (peaks) obtained on MEs 1 to 9, after the passage of a bubble, for two different inclination angles of the electrode.

It was noticed that, for a bigger inclination, the length of the hops becomes smaller. The bubble rises gliding over the electrode from 40° inclination. Figure 13 shows the peak current registered on ME 6 after the passage of a bubble when the electrode had an inclination of 50°. The current peak maxima registered on the nine MEs are presented in Fig. 14.

Figure 15 shows the ratio of the height of the peaks and the natural convection current, averaged for the nine MEs, as a function of the electrode inclination angle. Figure 15 shows a maximum for 40° inclination. This corresponds to the angle at which the bubble stops bounding on the wall during its rise. For angles below 40°, the bubble may induce a very strong perturbation at the point where it hits the electrode, but its effect is weaker. For angles greater than 40° the ascent velocity of the bubble decreases with increase in inclination, reducing its effect.

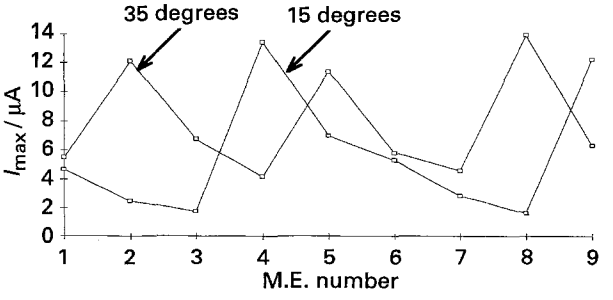

Fig. 12. Current peaks on the nine MEs. ($D_{eq} = 2.2$ mm).

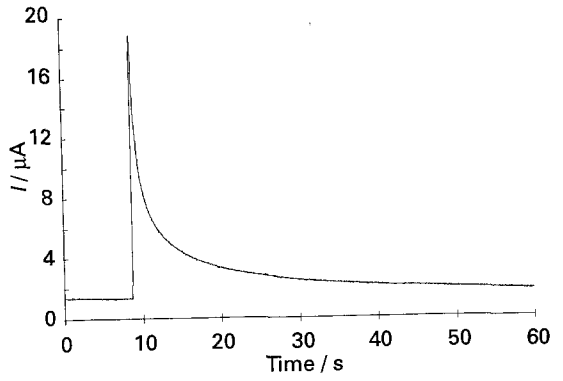

Fig. 13. Current signal on the ME6 after the rise of a bubble. ($D_{eq} = 2.2$ mm, $\alpha = 50°$).

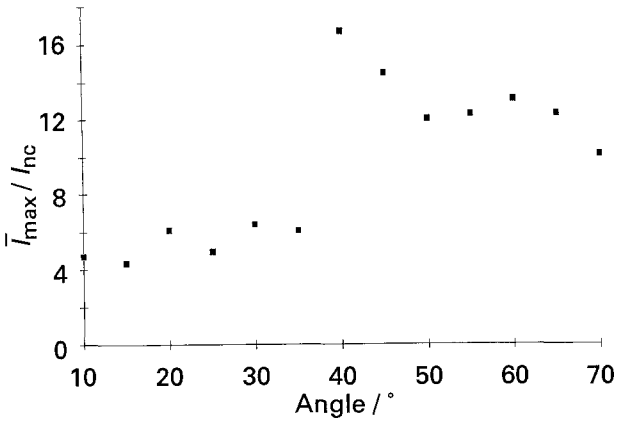

Fig. 15. Average I_{max}/I_{nc} against inclination angle. ($D_{eq} = 2.2$ mm).

Figure 16 shows the averages of I_{max}/I_{nat} on the nine MEs for several bubble diameter and electrode inclinations, in the form of a three-dimensional graph. A maximum at 16.6 occurs for a bubble of equivalent diameter 2.2 mm, and an electrode inclination of 40°.

For the bubble with maximum effect, Fig. 17 shows the current registered on a ME as a function of $t^{-0.5}$, where $t = 0$ is the time when the bubble passes in front of the ME. If the bubble dries the electrode as it passes by, a straight line would be obtained with an identical slope to that obtained from the response of the ME to a sudden potential jump, in the zone of natural convection limiting current. The observed curvature indicates that a liquid film remains between the electrode and the bubble. Even for this optimal case, the liquid at the electrode surface is not totally renewed. This can also explain the diminution of I_{max} on the MEs when the equivalent diameter of the bubble is greater than 2.2 mm. In fact, the bubbles become more flexible and it is possible that they penetrate less deeply into the diffusion layer.

3.3. *Local perturbation on a vertical electrode*

Mass transfer enhancement by a stream of micro bubbles was studied by Tobias *et al.* [16] using a micromosaic electrode. The stream was generated electrolytically and could rise either inside or outside the mass transfer boundary layer (approximately 150 μm thick). The mass transfer resulting from bubbles rising within this layer was found to be strong and localized, as predicted by the surface renewal theory. Meanwhile a steady laminar enhancement was observed when bubbles rose outside it.

The perturbation intensities caused by bubbles of higher volume depend upon the geometry and the nature of the bubble wake. These can be classified according to the bubble Reynolds number in three categories [22, 23]. For low Reynolds numbers the streamlines followed the interface. At intermediate Reynolds numbers the streamlines separate from the surface and form a laminar closed region immediately behind the bubble. At even higher Reynolds numbers, the wake becomes progressively turbulent and begins exchanging liquid with the external medium by a vortex shedding mechanism.

The Reynolds numbers at which these transitions occur are well known for high M-liquids. Here flow visualization, using techniques such as hydrogen bubble tracers, is easier to realize than in low M-liquids because of the stabilizing effect of viscosity [22].

Figure 18 shows a photograph of a two-dimensional bubble whose equivalent diameter is 9.5 mm. Its

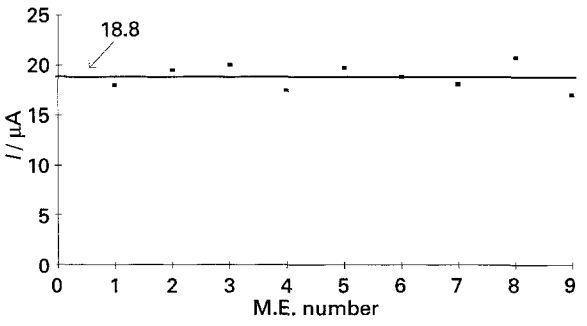

Fig. 14. Current peaks on the nine MEs after the rise of a bubble. ($D_{eq} = 2.2$ mm, $\alpha = 50°$).

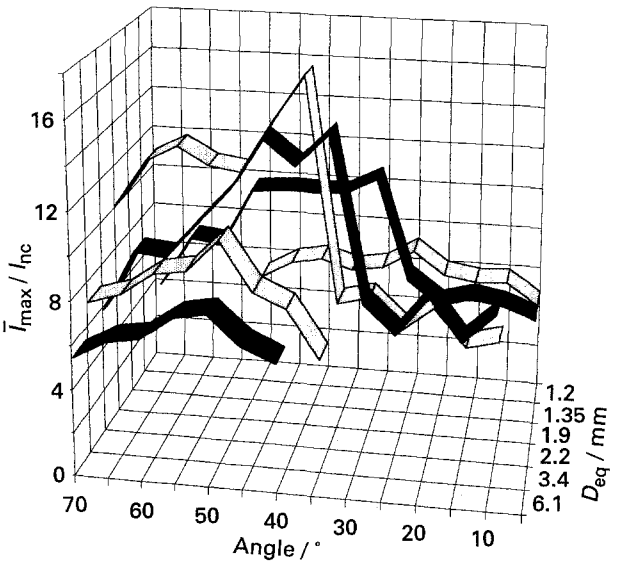

Fig. 16. Average I_{max}/I_{nc} against equivalent diameter and inclination angle.

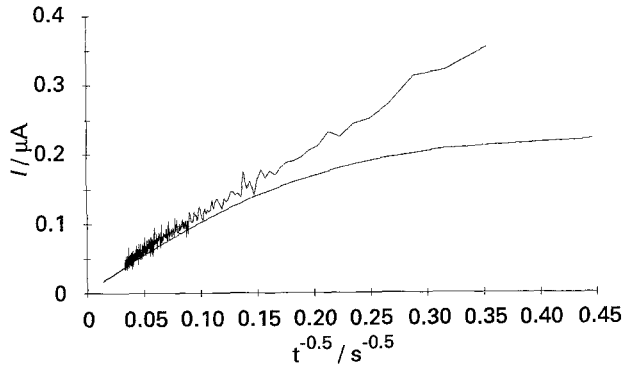

Fig. 17. Comparison with surface renewal mechanism.

wake and path were visualized using hydrogen bubble tracers. Such photographs were taken in a 60 cm × 10 cm × 0.8 cm Plexiglas® cell. Hydrogen microbubbles were electrogenerated by means of a Nickel wire (0.1 mm diameter) cathode. If the bubble was rising according to the present experimental conditions (i.e. without wall effects and in a liquid whose physical properties were not affected by the presence of hydrogen micro bubbles), its Reynolds number would be 1450.

A schematic interpretation of the two-dimensional wake flow is presented in Fig. 19. In spite of the different degree of instability dictated by the cell walls, it reflects a cross section of the three-dimensional wake configuration. Figure 19 shows a cyclic vortex formation-shedding process experienced by the bubble. This mechanism was qualitatively described by Rigby and Capes [24] and recently by Tsuchiya and Fan [23], who also proposed a model to interrelate the vortex-shedding frequency and the primary wake size [25] for bubbles with Reynolds numbers between 800 and 10^4. Nevertheless, even if the liquid perturbation intensity around the moving bubble is too weak to be treated through tracer visualization, the periodic nature of asymmetric wake shedding is without doubt the cause of both helicoidal motion of spheroid bubbles and of the spherical bubble cap pendular motion.

For bubbles having low Reynolds numbers analysis of the formation-shedding process through the current enhancement measured with the system of MEs was used. Experiments were done in order to relate measured current peaks to bubble volumes and to separation distances. As well as signals identical to those shown in Fig. 11, both the bubble transverse diameter and the position in the ME plan when the bubble crosses it, were determined for each experiment by means of a photograph. An example is shown in Fig. 20.

The bubble Reynolds numbers varied from 75 to 650. In a first series of experiments the nine MEs were positioned horizontally. Such an arrangement offers the advantage of simultaneous measurement of the perturbation width on the electrode. The perturbation height was determined from experiments in which this row was in a vertical position.

Fig. 18. Example of the wake and path of a two-dimensional bubble. (Re = 1450).

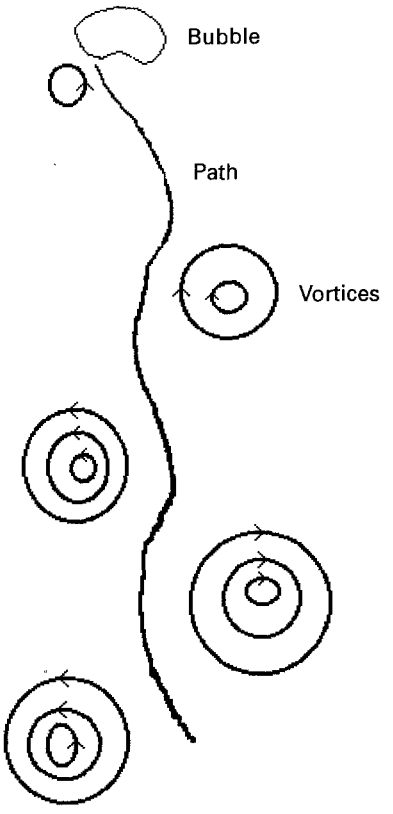

Fig. 19. Schematic interpretation of the wake flow of a two-dimensional bubble. (Re = 1450).

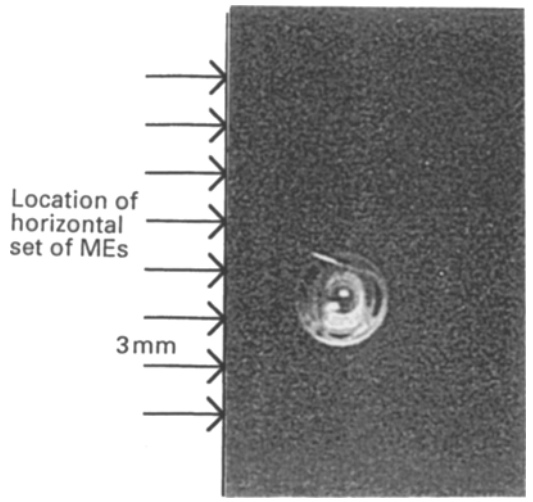

Fig. 20. Bubble transverse diameter and position in ME plan.

4. Conclusion

As indicated in the introduction, it was not possible to model quantitatively the relationships between local currents and fluid flows. This difficulty arises from the asymmetric effect of the electrode on the pressure field. In fact, when the bubble rises close to the wall, the degree of wake instability is higher than when it rises in the cell centre. Efforts are currently in progress to analyse the information statistically. Nevertheless, the following conclusions have been clearly drawn from raw measurements: (a) Current peaks increase as a function of the Reynolds number of the bubble; no maxima appear as noted for inclined electrodes. (b) Within a certain distance from the electrode wall, the position of the bubble in the ME plan appears to have a weak effect on the peak height. This distance depends on the Reynolds number. (c) The current does not increase over the whole height of the electrode, but on a limited zone. However, the height of the perturbed surface remains greater than its width. (d) For big bubbles, the presence of two distinct perturbed zones was sometimes observed. This is related to vortices shed from both sides of the bubble.

Acknowledgement

The authors are grateful for the generous help of Arturo Araque. The research was supported by the Swiss National Foundation for Scientific Research.

References

[1] N. Ibl, *Chem. Ing. Techn.* **35** (1963) 353.
[2] G. M. Cook, *AIChE Symposium Series* **74** (1978) 140.
[3] N. Ibl, E. Adam, J. Venczel and E. Schlach, *Chem. Ing. Techn.* **43** (1971) 202.
[4] N. Ibl and J. Venczel, *Metalloberfläch* **24** (1970) 365.
[5] N. Ibl, R. Kind and E. Adam, *An. Quim.* **71** (1975) 1008.
[6] L. Sigrist, O. Dossenbach and N. Ibl, *Int. J. Heat Mass Transfer* **22** (1979) 1393.
[7] D. J. Economou and R. C. Alkire, *J. Electrochem. Soc.* **132** (1985) 601.
[8] G. H. Sedahmed, H. A. Farag, A. A. Zatout and F. A. Katkout, *J. Appl. Electrochem.* **16** (1986) 374.
[9] O. N. Cavatorta and U. Böhm, *ibid.* **17** (1987) 340.
[10] S. Piovano, O. N. Cavatorta and U. Böhm, *ibid.* **18** (1988) 128.
[11] O. N. Cavatorta and U. Böhm, *Chem. Eng. Res. Des.* **66** (1988) 265.
[12] *Idem, J. Appl. Electrochem.* **21** (1991) 40.
[13] A. Shah and J. Jorne, *J. Electrochem. Soc.* **13** (1989) 144.
[14] W. Kast, *Chem. Ing. Techn.* **35** (1963) 785; *Int. J. Heat Mass Transfer* **5** (1962) 329.
[15] W. D. Deckwer, *Chem. Eng. Sci.* **35** (1980) 1341.
[16] C. W. Tobias, *AIChE J.* **34** (1988) 1981.
[17] P. Larpin, Thesis no 465, EPF Lausanne (1982).
[18] D. C. Blanchard and L. D. Syzdek, *Chem. Eng. Sci.* **32** (1977) 1109.
[19] P. Grassmann, 'Physical Principles of Chemical Engineering', Pergamon Press, Oxford (1974).
[20] S. W. Sears and R. A. Hartunian, *J. Flyuid Mech.* **3** (1957) 27.
[21] W. L. Haberman and R. K. Morton, *Amer. Soc. Civ. Eng.* Paper 2799 (1954) 227.
[22] D. Bhaga and M. E. Weber, *J. Fluid. Mech.* **105** (1981) 61.
[23] L. Fan and K. Tsuchiya, *Chem. Eng. Sci.* **43** (1988) 1167.
[24] G. R. Rigby and C. E. Capes, *Can. J. Chem. Eng.* **48** (1970) 343.
[25] L. Fan and K. Tsuchiya, *Chem. Eng. Sci.* **43** (1988) 2893.